Experimental investigation on multiscale hydrodynamics in a novel gas-liquid-solid three phase jet-loop reactor

Yongxiang Gao[1], Xi Gao[2], Du Hong[1], Youwei Cheng[1,], Lijun Wang[1], Xi Li[1]*

1. College of Chemical and Biological Engineering, Zhejiang University, Hangzhou, Zhejiang 310027, P.R. China

2. National Energy Technology Laboratory, Morgantown 26505, WV, United States

Abstract

Multiphase flow hydrodynamics in a novel gas-liquid-solid jet-loop reactor (JLR) were experimentally investigated at the macro- and meso-scales. The chord length distribution was measured by an optical fiber probe and transformed for bubble size distribution through the maximum entropy method. The impacts of key operating conditions (superficial gas and liquid velocity, solid loading) on hydrodynamics at different axial and radial locations were comprehensively investigated. JLR was found to have a higher solid loading capability than slurry bubble column on the premise of the same overall gas holdup. The gas holdup, axial liquid velocity and bubble velocity increase with gas velocity, while liquid velocity has little influence on them. Compared with the gas-liquid JLRs, solids decrease the gas holdup and liquid circulation, reduces the bubble velocity and delays the flow development due to the enhanced interaction between bubbles and particles (Stokes number>1). This work also provides a benchmark data for CFD model validation.

Topical Heading: Transport Phenomena and Fluid Mechanics

* To whom correspondence should be addressed. E-mail: ywcheng@zju.edu.cn

Tel: +86-571-87952210, Fax: +86-571-87951227.

Keywords: Jet-loop reactor; Hydrodynamics; Bubble behavior; Bubble size distribution; Optical fiber probe; Maximum entropy method.

Introduction

Jet-loop reactors (JLRs) consist of modified bubble columns with a draft tube that divides the entity into two regions, a riser and a downcomer, and gas or/and liquid injection nozzles to supply excellent solid suspension. JLRs are efficient apparatuses for industrial processes, especially those with high solid concentration such as wastewater treatment, aerobic fermentation and hydrocracking of heavy oil.[1,2]

Three phase JLRs (gas-liquid-solid) are novel compared to the relatively widely studied gas-liquid bubble column,[3] gas-liquid airlift reactor,[4] gas-liquid JLRs,[5,6] gas-liquid-solid bubble column[7,8] or gas-liquid-solid airlift reactor.[9,10] Recently, studies on JLRs were mostly relevant to gas-liquid two-phase flow,[11-16] while gas-liquid-solid three-phase systems were rarely studied, in comparison.[17-21] Fan et al.[17] distinguished three flow modes (packed bed, fluidized bed and circulated bed mode) according to the solids suspension performance in a JLR. They found the overall gas holdup and liquid circulation velocity increased when the superficial gas and liquid velocity increased. Padmavathi and Rao[18] reported that increasing solids loading and particle density reduced the overall gas holdup and liquid circulation velocity. Some design considerations on JLRs were carried out by Hwang and Fan[19] and Pironti et al.,[20] in which they discussed the effect of draft position on overall gas holdup. Most experiments on gas-liquid-solid three-phase JLRs were focused on macro-scale hydrodynamics, such as gas holdup, liquid circulation velocity, etc. The flow space distributions and mesoscale hydrodynamics, like bubble size distribution (BSD), bubble/liquid velocity distribution and

solid holdup distribution are distinctly deficient, but they are of great significance for mixing and mass transfer. Compared to gas-liquid bubble column, gas-liquid airlift reactor or gas-liquid JLR, the introduction of solids into the gas-liquid system increases the complexity of dynamic properties among phases, both at the macroscale and mesoscale. Further, the effect of solids on flow hydrodynamics is still under controversy for slurry bubble columns,[22-26] as well as for three-phase JLRs.

Mass transfer in the JLR is highly related to the gas-liquid interfacial area. Thus, it is essential to control the knowledge of gas holdup and bubble size for successful industrial scale-up. Measuring bubble behavior in a JLR is difficult due to the complicated circumstance, especially when the solid phase exists. There are two main measuring methods: invasive and non-invasive techniques.[27] Non-invasive techniques, such as dynamic gas disengagement (DGD)[28] and the photographic technique,[29] like the endoscope technique,[30] are limited because of some ineluctable hypotheses or strict measuring conditions, such as the requirement of a quasi-2D apparatus, although they could be the "standard" against other techniques. Hence, the invasive techniques, like needle probes, are preferred for bubble behavior studies, such as those that investigate local gas holdup, bubble frequency, bubble velocity and bubble diameter.[4,31-35] In a system containing solid particles, the optical-based techniques, such as the focused beam reflectance method,[30] are more practical than other needle probes that pierce bubbles. However, two or more probes are required for bubble diameter and bubble velocity calculation. Because of the random movement of bubbles, the bubble size measured by needle probes is generally the bubble chord length. Therefore, an efficient method is needed to transform the bubble chord length distribution (CLD) to BSD for a correct prediction of the interfacial area. Clark and

Turbon[36] pioneered the backward transformation by a discretization method, but the technique was cumbersome. Liu and Clark[37] improved the backward transformation through a predictive Parzen window to estimate BSD. Overall, the main drawbacks of the backward transformation method are the unpredictability of the presupposed BSD (Gamma or Rayleigh distribution) and the need for large data to obtain a correct result. Later, Santana et al.[38] proposed the maximum entropy method, which needs fewer samples to get numerical stable results compared to the backward transformation. Moreover, various shape factors should be considered during the calculation of BSD because of its distinct change with the Reynolds, Morton and Eötvös numbers.

The purpose of this paper is to fill in the knowledge gap of the hydrodynamics on the gas-liquid-solid three phase JLR, both at the macro- and meso- scales. As discussed above, JLR is a very promising multiphase reactor for some important industrial processes. However, few experimental investigations are available in the literature. Some experiments on gas-liquid-solid three-phase JLRs were only focused on macro-scale hydrodynamics, such as gas holdup, liquid circulation velocity, etc. The flow space distributions and mesoscale hydrodynamics, like bubble size distribution (BSD), bubble/liquid velocity distribution and solid holdup distribution are distinctly deficient, but they are of great significance for mixing and mass transfer. Furthermore, industrial reactors usually contain solids, which increases the complexity of flow hydrodynamics. Specifically, to give a pertinent guideline for the hydrocracking of the heavy oil, low superficial gas and liquid velocities are considered with a wide range of solid concentration (0~30 vol.%). A dual-tip needle probe, called an optical fiber probe, is employed to predict the bubble behaviors, including the local gas holdup, bubble frequency, bubble

diameter and bubble velocity. BSD is obtained by the maximum entropy method. The effects of the superficial gas velocity, liquid velocity and solid loading on flow distributions are discussed. This work first analyzes the local hydrodynamics and their distributions in a gas-liquid-solid three phase JLR, which provide a benchmark data for the industrial scale-up and CFD model validation.

Experimental setup

Reactor configuration

A schematic diagram of the experimental gas-liquid-solid three phase JLR is shown in Figure 1. The reactor made from Plexiglas, with an inner diameter (I.D.) of 0.186 m and 2.5 m height, includes four sections: a conical bottom of 0.173 m height and 60 degree cone angle, a riser section of 0.1 m I.D. and 1.4 m height, a downcomer section mounted concentrically with the riser, and a gas-liquid-solid separator at the top. A specially designed nozzle with 10 mm I.D. (see Figure 1) is located at the bottom of the reactor. A tube of 6 mm I.D. with 1 mm thickness is welded concentrically with the nozzle. More details on the geometry parameters can be found in our previous work.[5]

Clean gas (ρ_g=1.2 kg·m^{-3}, μ_g=1.8×10^{-5} Pa·s) from the air compressor was injected into the reactor through the outer part of the nozzle, while water (ρ_l=998 kg·m^{-3}, μ_l=1.0×10^{-3} Pa·s) from the reservoir was injected into the reactor through the inner part. The bed was partially filled with transparent glass beads with a density of 2400 kg·m^{-3} and a Sauter mean diameter of 630 μm measured by a Malvern laser particle size analyzer. Solid particles were suspended by the liquid and gas flows, mainly circulated between the riser and downcomer sections. The gas flow was discharged into the environment after the gas-liquid-solid separator, while water is

rerouted back to the reservoir.

The effects of different gas superficial velocity, liquid superficial and solid loading on flow hydrodynamics at the macro- and meso- scales were investigated at different axial and radial locations. The superficial velocity of the gas and liquid phases are calculated based on the cross-sectional area of the JLR and the solid loading is defined as the solid volume fraction of the total solid and liquid volume when gas is absent. Experimental operating conditions and measurement locations are summarized in Table 1.

Measuring methods and data processing

Bed expansion

The bed expansion method [5,39,40] is a prevailing technique to measure the overall gas holdup, which is simpler and more effective than the high-speed camera method. The image analysis is cumbersome and it is difficult to count the number of bubbles in a three-dimensional apparatus when the gas holdup is relatively high. The bubbles overlapped with each other cause trouble for the analysis of the bubble's volume or area. The overall gas holdup in the JLR was obtained by the following equation:

$$\overline{\varepsilon_g} = \frac{H_d - H_s}{H_d} \tag{1}$$

where H_d is the dynamic height of bed surface during the experiment and H_s is the static height after fast-shutting the gas and liquid valves simultaneously. During the experiment, strong oscillations of the dynamic height were observed. Therefore, three tests were conducted in each operating condition, and the average value was utilized to estimate the overall gas holdup.

Sample withdraw method

The sample withdraw method was commonly employed to measure solid holdup.[40-43] A stainless tube of 6 mm I.D. mounted in a silicon cork was designed to conveniently move the sample at various axial heights. For each run, a small amount of slurry was discharged previously to eliminate the effect of solids aggregation in the tube and 7-9 ml slurry was then discharged for analyzing. The solid holdup, namely the solid concentration in the slurry phase, was measured by the filtering-drying technique.[40,43] Thus, the solid holdup is calculated as follows:

$$\varepsilon_s = \frac{m_s/\rho_s}{m_s/\rho_s + (m_{sl} - m_s)/\rho_l} \tag{2}$$

where m_{sl} and m_s are the mass of solid-liquid slurry and solids, respectively. Five samples were analyzed to get an average value for each run, and their relative errors were within ±10%.

Pavlov tube

The axial liquid velocity was measured by the Pavlov tube. Pavlov tube is similar to Pitot tube[44] and made from a stainless tube with an outer diameter of 6 mm. A sheet metal divides the tube into two independent parts, and a hole (1 mm) is drilled at each side within 4 mm apart. Its detailed structure is depicted in our previous work by Li et al.[45] The measured differential pressure between the two holes is transformed to the voltage signal through a data acquisition card. Note that, water is used to purge the tube before every normal test to prevent the effect of bubbles and particles. The purge time is 20 s. The sample time and frequency are 60 s and 135 Hz, respectively. The time-averaged axial liquid velocity, u_l, is calculated by a revised formula within the consideration of the gas and solid holdup:[45]

$$u_l = \frac{1}{n}\sum_{i=1}^{n} u_i \text{ with } u_i = \begin{cases} \sqrt{\dfrac{2\Delta P_i}{K\left(\varepsilon_g \rho_g + J\varepsilon_l \rho_l\right)}} & \text{if} \quad \Delta P_i \geq 0 \\ -\sqrt{\dfrac{2\Delta P_i}{K\left(\varepsilon_g \rho_g + J\varepsilon_l \rho_l\right)}} & \text{if} \quad \Delta P_i < 0 \end{cases} \tag{3}$$

where $J = 1 + \varepsilon_g$ is the momentum transfer factor, and $K = 1.56/\left(1 + 0.5\varepsilon_s\right)$ is a correction factor, obtained from a calibration experiment. For each operating condition, three tests were conducted to get an average value.

Optical fiber probe

An optical fiber probe was introduced to investigate the bubble behaviors. The PV6D optical fiber probe was utilized in this study, which is a kind of reflective-type optical fiber probe, produced by the Institute of Process Engineering, Chinese Academy of Science. PV6D consists of two 1×1 mm optical fiber arrays, and each array contains emitting and receiving quartz fibers. The distance between the two arrays is 1.95 mm. The optical fiber arrays are covered by a stainless steel sleeve with 4 mm O.D. and 400 mm length. A thin glass hood is used to enshroud the probe tips to prevent excessive wear. More details can be found in Li et al.[46]

The PV6D was successfully employed in different flows by many researchers. Gao et al.[47] used PV6D in a turbulent fluidized bed to investigate solid concentration. Razzak et al.[48] expanded PV6D to a three-phase circulating fluidized bed for gas holdup exploration. The intrinsic reason for this reflective-type optical fiber probe in measuring solid or gas holdup is that the received light intensity is different in different mediums due to their different refractive index. The received light is inverted to the voltage signal after multiplying by the photo-multiplier. The gas phase reflects the highest voltage because of its lowest refractive index. The

representative signals produced in the gas-liquid system and gas-liquid-solid system were shown in Figure 2. This figure shows segment normalized signals in 0.4 s. Figure 2a shows that the gas phase obtains the strongest signal, while the liquid phase obtains the weakest, near-to-zero signal. The introduction of solid particles does not change this kind of characteristic, but increases the fluctuation of the baseline in a small range as shown in Figure 2b. Therefore, it is feasible to distinguish the gas phase from others by the PV6D method. The optimal measuring parameters according to some preliminary experiments are as follows: sampling frequency, 5000 Hz, data length, 131072. Five samples were taken for each measuring position.

It is crucial to determine the correct bubble signal from the raw signal. Bubble signal manifests high voltage in the whole signal, hence a reasonable and accurate threshold is needed. Lo et al.[49] set a constant threshold according to the highest level signal intensity directly. Liu et al.[50] judged the bubble by visual examination of the signals. Sobrino et al.[51] and Acosta-Iborra et al.[52] determined the threshold by plotting the probability density function (PDF) of the voltage. In view of the raw signal, e.g., Figure 3a, the baseline is time-varying, revealing the difficulty in judging the bubble signal by a constant threshold. In this study, we utilized the PDF method to determine bubbles. As shown in Figure 3b, a peak exhibited in PDF represents the liquid and solid phase, while the tail in relatively high voltage represents bubbles. A bubble is detected when the tail begins and the slope of the histogram approximates to zero. In this way, all signals larger than the threshold represent the gas phase, as shown in Figure 3a. The leading probe is utilized to calculate the local gas holdup.

$$\varepsilon_g = \frac{\sum t_i}{T} \tag{4}$$

where t_i represents the passing time of a bubble through a probe tip, T is the whole sample

time.

The local bubble frequency is calculated by:

$$f = \frac{N_b}{T} \tag{5}$$

where N_b is the total number of bubbles.

We apply a cross-correlation algorithm to obtain the local bubble velocity.

Step 1: Divide data (131072 in this study) into N segments of equal data length. N =32 is recommended in this study, and its impact on the results was discussed in Appendix A.

Step 2: For each segment, calculate cross-correlation function ($R_{xy}(\tau_i)$):

$$R_{xy}\left(\tau_i\right) = \lim_{T_i \to \infty} \frac{1}{T_i} \int_0^{T_i} X\left(t\right) Y\left(t+\tau\right) dt \tag{6}$$

where $X(t)$ and $Y(t)$ represent the signals detected by the leading and rear probe, respectively. T_i is the testing time of a segment. When $R_{xy}(\tau_i)$ reaches the maximum, the corresponding τ_i is dwelling time of the bubble passing through probes, as shown in Figure 3c. Thus, the bubble velocity for a segment is calculated by:

$$u_{bi} = \frac{L}{\tau_i} \tag{7}$$

where L is the distance between the two probe tips, 1.95 mm in this study.

Step 3: Calculate the time-averaged bubble velocity as follows:

$$u_b = \frac{\sum_{i=1}^{N} u_{bi} \varepsilon_{gi} R_i}{\sum_{i=1}^{N} \varepsilon_{gi} R_i} \tag{8}$$

where ε_{gi} and R_i represent the local gas holdup and cross-correlation coefficient for each segment, respectively.

The chord length for each bubble is calculated:

$$l_{bi} = u_{bi} t_i \tag{9}$$

It is noted that the same bubble velocity u_{bi} is utilized for different bubbles in a segment. In reality, bubbles may deform and rise in a random direction; thus, some erroneous bubbles can also be found, which are eliminated necessarily.[51] A measured bubble chord length smaller than L and larger than the reactor diameter is rejected.

It is known that only the bubble chord length distribution (CLD) can be obtained from the optical fiber probe since the probes do not always pierce the bubble center. Thus, an inversion from CLD into BSD is necessary. In this study, the maximum entropy method proposed by Santana et al.[38] is employed to get the BSD, which needs smaller bubble samples when compared with the traditional method (backward transform, proposed by Liu and Clark[37]). The maximum entropy method is based on the Shannon entropy principle. When the Shannon entropy function reaches the maximum with the constraints in Eq. 10, the PDF of the bubble diameter is determined.

$$\begin{aligned} &\max_{p(\mathrm{D})} \int_{D\in\Delta} -p(D)\ln\left(p(D)\right) dD \\ &s.t.\ \int_{D\in\Delta} p(D) dD = 1 \\ &\quad \int_{D\in\Delta} D^i p(D) dD = \left\langle D^i \right\rangle, i = 1,\ldots,K \end{aligned} \tag{10}$$

where $p(D)$ is the PDF of bubble diameter, Δ is the interval variation of the D (the bubble diameter), and $\left\langle D^i \right\rangle$ is the ith raw moment of bubble diameter, which can be estimated from the raw moment of the sample, $m_i(D)$, as follows:

$$m_K(D) = \frac{K+2}{2N_b} \sum_{j=1}^{N_b} \left(\frac{l_{bj}}{\varphi} \right)^K \tag{11}$$

where φ is the shape factor, defined by the ratio of the minor to the major axis of a bubble. In this study, we employ the correlation proposed by Bozzano and Dente[53] to evaluate the shape

factor, which takes *Eo* number and *We* number into account:

$$\varphi = \frac{10\left(1+1.3Mo^{1/6}\right)+Eo}{10\left(1+1.3Mo^{1/6}\right)+3.1Eo} \tag{12}$$

The solution of Eq. 10 was given by Santana et al. [38] as:

$$p_K\left(D,\lambda\right) = \exp\left(\sum_{i=1}^{K}-\lambda_i\left(D^i-m_i\left(D\right)\right)\right)\Big/\int_{D\in\Delta}\exp\left(\sum_{i=1}^{K}-\lambda_i\left(D^i-m_i\left(D\right)\right)\right)dD \tag{13}$$

where λ_i is the Lagrange multiplier for the *i*th raw moment constraint, which can be obtained iteratively as:

$$\lambda^{(k)} = \lambda^{(k-1)} - H^{-1}\left(\lambda^{(k-1)}\right)G\left(\lambda^{(k-1)}\right) \tag{14}$$

where *H* and *G* are the Hessian matrix and the gradient vector of the *Q*, respectively, calculated as:

$$H_{ij}\left(\lambda^{(k-1)}\right) = \frac{\partial Q\left(\lambda^{(k-1)}\right)}{\partial\lambda_i\partial\lambda_j} = \int_{D\in\Delta}\left(D^i-\left\langle D^i\right\rangle\right)\left(D^j-\left\langle D^j\right\rangle\right)p_K\left(D,\lambda^{(k-1)}\right)dD \tag{15}$$

$$G_i\left(\lambda^{(k-1)}\right) = \frac{\partial Q\left(\lambda^{(k-1)}\right)}{\partial\lambda_i} = \int_{D\in\Delta}\left(D^i-\left\langle D^i\right\rangle\right)p_K\left(D,\lambda^{(k-1)}\right)dD \tag{16}$$

Herein, *Q* is the potential function to be minimized, given by:

$$Q_K\left(D,\lambda\right) = \int_{D\in\Delta}\exp\left(\sum_{i=1}^{K}-\lambda_i\left(D^i-\left\langle D^i\right\rangle\right)\right)dD \tag{17}$$

The detailed calculating procedure can be found in Santana et al.[38] or Tyagi and Buwa.[34]

Finally, with the BSD obtained by Eq. 13, the mean bubble diameter can be calculated by:

$$d_b = \int_0^{+\infty} p\left(D\right)DdD \tag{18}$$

High-speed camera

Image analysis as a non-invasive method, is widely used to measure bubble size and velocity,[29,33,54] but it can only be applied to a system with simple geometry. To validate the feasibility of optical fiber probe in measuring the bubble velocity and diameter, experiments in

a 2-D bubble column of 1.5 m (height) × 0.15 m (width) × 0.05 m (depth) were carried out using an optical fiber probe and a high-speed camera. The schematic diagram of the 2-D bubble column is shown in Figure 4a. A needle sparger is located at the base, which consists of 45 capillary tubes of 0.51 mm I.D. and 10 cm length in a rectangular arrangement with three arrays, as shown in Figure 4b. Both an optical fiber probe and a high-speed camera (Mikrotron Cube 7) (operated with the resolution of 1024×1024 pixels and 500 frames per seconds (fps)) were utilized to obtain the experimental bubble velocity and bubble diameter at the height of 60 cm above the sparger. The static height of water remained at 100 cm during experiments, while the superficial gas velocity changes were in the range of 0.0092-0.0287 m/s. As shown in Figure 4c, experiments were operated in the homogeneous flow regime in order to produce uniform bubbles, avoiding the bubble overlap and coalescence. All parameters of optical fiber probe were same as the experiments in the JLR.

In this study, 300 bubbles in 30 photos were sampled to obtain BSD and bubble velocity by Image-Pro Plus 6.0 software. The centroid distance of the two consecutive photos is divided by the bubble rising time (0.004 s) to get the bubble rising velocity.

Results and discussion

Validation of optical fiber probe using a high-speed camera

The measurement of bubble dynamics by a high-speed camera is more direct than an optical fiber probe. The high-speed camera is also believed to be fundamentally more accurate and can be used to validate the optical probe. Figure 5 presents the bubble velocity PDF and BSD measured by both an optical fiber probe and a high-speed camera at U_g=0.0287 m/s. Both for bubble velocity PDF and BSD, their shapes measured by optical fiber probe and camera are

similar and their curves are overlapped partially. Compared with the bubble diameter measured by the high-speed camera, a possible reason for overestimated prediction of bubble diameter by optical fiber probe is that fairly small bubbles are unable to be detected by the optical fiber probe.

The comparison of mean bubble velocity and bubble diameter measured by an optical fiber probe and a high-speed camera at various superficial gas velocities is summarized in Table 2. The deviations of both bubble velocity and bubble diameter between the optical fiber probe and the high-speed camera are less than $\pm$20%, which reveals the feasibility and accuracy of the optical fiber probe in predicting the bubble behaviors.

Overall behavior

Figure 6 presents the effect of solid loading (C_s) on overall gas holdup ($\overline{\varepsilon_g}$) and liquid circulation velocity (u_{cir}) at U_g = 0.085 m/s, U_l=0.01 m/s. With the increasing of solid loading, $\overline{\varepsilon_g}$ first decreases dramatically then levels off. Similar results were observed by other researchers.[55-57] The reason for this phenomenon is that, when C_s increases, the bubble coalescence rate increases, resulting in the decreasing of the gas momentum per unit mass slurry. Thus, the gas holdup decreases. However, relatively high C_s enhances the breakup probability of bubbles. This flat trend at C_s>15 vol.% implies that the competition between bubble coalescence and breakup reaches an equilibrium. It is worth noting that, in this JLR system, the equilibrium point (C_s=15 vol.%) is higher than that (C_s=10 vol.%) reported in a slurry bubble column by Rabha et al.,[22] which reveals that, JLRs have a higher solid loading capability, with the same overall gas holdup, due to its excellent solid suspension ability (see Figure 8). Figure 6 also depicts that increasing solid loading reduces the liquid circulation

velocity because of an increase of the mixture viscosity, which is consistent with the result reported by another study,[57] and the axial liquid distributions (see Figure 10) can also interpret this phenomenon.

Solid holdup distribution

The radial profiles of solid holdup at different bed heights at U_g = 0.125 m/s, U_l =0.01 m/s, C_s=30 vol.% is depicted in Figure 7. In both the riser and downcomer xiregions, solids seem to accumulate near the wall, but the discrepancy between column center and the wall is not obvious, which agrees with the observation of Razzak et al.[58] This phenomenon owes to the bubble coalescence, the wall effect and the back mixing. More large bubbles at the center contribute to the solids entrainment due to the bubble wake. The wall effect makes larger friction of solids near the wall, which enhances the solid back mixing as well, thus more solids accumulate near the wall. Figure 7 also reveals that, the solid holdup at the separator section is lower than the internal loop region and its radial distribution is more uniform. The reason is that the flow velocity decreases when entering the separator section where a sudden expansion area exists, which leads to deficient energy for solids suspension. However, this feature is beneficial for the industrial reactor to prevent the solids from being carried out of the reactor.

Figure 8 shows the effects of U_g and U_l on the axial solid holdup distribution (the conical section (region I) is not tested) at C_s=30 vol.%. Obviously, the solids are nearly evenly distributed in the internal loop region (region II) and decrease dramatically in the separator section (region III), which reveals that the JLR has an excellent solids suspension ability, thus avoiding hot spot and coking. In addition, increased superficial gas velocity and liquid velocity contribute to solids suspension, owing to the enhancement of liquid circulation velocity.[5]

Figure 9 shows the effect of solid loading on radial profiles of solid holdup at H=0.65 m. An increase of solids loading increases the radial solid holup, while does not significantly change the shape of radial distribution (namely, slightly higher solid holdup near the wall). In addition, solids are completely suspended in the column at various solid loadings.

Liquid velocity distribution

Figure 10a-c shows the radial profiles of the axial liquid velocity considered the effects of different operating conditions including U_g, U_l and C_s, respectively. In general, the distinct characteristic of upward flow in the riser and downward flow in the downcomer is maintained in the JLR, which leads to a regular internal flow circulation.

With the increasing of U_g, the axial liquid velocity increases, as shown in Figure 10a. A similar result is obtained in our previous work in a JLR without solids.[5] This is because, for the bubble- (or liquid) driven flow, more gas injection (liquid injection rate keeps constant) causes a faster slurry circulation rate. Figure 10b reveals that increasing U_l hardly changes the axial liquid velocity in either magnitude or distribution. Interestingly, a distinct increase of axial liquid velocity was observed under gas-liquid co-injection (with U_l) when compared with gas jet alone mode (without U_l) in our previous work.[5] The present gas-liquid-solid JLR (with U_l) is conducted in a coalesced bubble flow regime with complete fluidization,[59] while partial fluidization is observed when U_l=0. Thus, a conclusion can be drawn that, the effect of U_l on axial liquid velocity is weak when the particles are completely fluidized in a gas-liquid-solid JLR. Figure 10c presents the effect of solid loading on axial liquid velocity. The axial liquid velocity decreases with the increasing of solids loading. A reasonable interpretation is that additional energy is needed to suspend particles. Thus, the corresponding liquid circulation

velocity decreases (also see Figure 6).

Bubble behaviors

Local gas holdup

Figure 11a-c illustrates the effects of U_g, U_l and C_s on radial distributions of the local gas holdup, respectively. In the riser region, a higher U_g results in a higher local gas holdup and steeper distribution, while there is nearly no change in the downcomer (Figure 11a). It is known that only small bubbles can be dragged down into the downcomer.[60] Furthermore, a large portion of space in the downcomer is occupied by the solid phase when particles are internally circulated. Thus, the change of local gas holdup with different U_g in the downcomer is inconspicuous. Figure 11b reveals the weak effect of U_l on local gas holdup, which is in agreement with the observation of Akita and Yoshida.[61] The effect of C_s on local gas holdup is depicted in Figure 11c. It can be seen that, with an increase of C_s, local gas holdup decreases dramatically and its radial profile becomes flatter. According to the result reported by Krishna et al.,[62] gas holdup reduces because of the enhancement of coalescence rate with an increase of C_s. In addition, large bubbles tend to accumulate at the column center. As a consequence, the local gas holdup at center decreases more rapidly than that near the wall.

Figure 12 shows the axial development of local gas holdup at C_s = 5 vol.% and 30 vol.%. When C_s = 5 vol.%, the radial distribution of local gas holdup does not change until H=0.65 m (namely, the flow is full-developed), while it equals to H=0.9 m for C_s = 30 vol.%. Moreover, as shown in Figure 12b, a saddle distribution is observed at lower position in the riser (H=0.2, 0.4 m) at C_s = 30 vol.%, which implies a longer distance to reach a fully-developed flow. Therefore, a higher solid loading delays the flow to reach full-development.

Bubble frequency

Figure 13a-c shows the effects of U_g, U_l and C_s on radial profile of bubble frequency at H=1.15 m, respectively. In overall, in the riser, bubble frequency presents a monotonic decrease from column center to the wall, implying more bubbles gather at column center. Differently, bubbles distribute uniformly in the downcomer.

With the increase of U_g and U_l, more bubbles are produced in the riser region, while hardly any variation is observed in the downcomer region, as shown in Figures 13a,b. It is readily comprehensible that in a JLR operated in a gas-liquid co-injection mode, the enhancive energy input reinforces the break-up rate of bubbles at the inception phase.[5] The influence of C_s shown in Figure 13c implies that bubble coalescence rate increases significantly as solids loading increases from zero to 15 vol.% on account of the increased viscosity in the slurry phase.

Bubble diameter

The effects of U_g, U_l and C_s on bubble diameter at the axial position of 1.15 m are shown in Figures 14a-c, respectively, where the BSD at the column center is presented on the left side and the right side is the radial profile of mean bubble diameter. As shown in Figure 14a(i), with an increase of U_g, the BSD becomes wider and its peak shifts toward the higher bubble diameter, which implies larger bubbles engender. The change of mean bubble diameter in the riser (see Figure 14a(ii)) with U_g interprets the similar regularity. However, it is contrary to the cognition that higher U_g accelerates the bubbles break-up rate, thus results in a smaller bubble size.[33,63] The possible reason for this discrepancy is that, under present operating conditions, the JLR operates in pseudo-homogeneous flow regime,[5] where bubble coalescence is still dominant, which is in agreement with the observation by Besagni and Inzoli.[29] Figure 14b illustrates that

an increase of U_l brings about narrower BSD and smaller bubble diameter, owing to the enhancement of break-up rate. On the contrary, an increase of solid loading leads to faster bubble coalescence and larger bubble size, as shown in Figure 14c. Large bubbles accumulate at the center of the column, while small bubbles distribute near the wall and downcomer (Figure 14b). Moreover, when the operating conditions (including U_g, U_l and C_s) are changed, the bubble diameter at the column center varies dramatically compared with other radial positions, which implies the dynamics at column center is more sensitive to operating conditions. In particular, the bubble diameter in the downcomer keeps constant in the size range of 5-7 mm.

Figure 15 shows the BSDs at different radial positions in the riser (r/R= 0, 0.29, 0.48) and the downcomer (r/R= 0.77). A narrower BSD and small bubble size displacement trend of the BSD peak are observed from column center to the wall, which further verifies that larges bubbles readily move towards the column center.

Bubble velocity

Figure 16a-c shows the effects of U_g, U_l and C_s on bubble velocity at H=1.15 m, respectively. Obviously, bubbles rise upwards in the riser and flow downwards in the downcomer, which results in an internal circulation of bubbles, and it is in accordance with the dynamics of liquid flow (see Figure 10).

An increase of U_g results in higher bubble velocity, as shown in Figure 16a. Two aspects are responsible for this phenomenon: when U_g increases, the increased local gas holdup reduces the friction of bubbles movement because of the enhancive bubble wake effect (see Figure 11a); on the other hand, the liquid internal circulation is intensified (see Figure 10a). Figure 16b illustrates that the change of U_l has no remarkable effect on the bubble velocity, which is in

agreement with the result of Wang et al.[31] Bubble rise velocity is influenced by the liquid velocity, gas holdup and solid holdup.[31] Thus, it is reasonable that the bubble velocity remains unchanged with U_l due to the changeless of liquid velocity and gas holdup (see Figure 10b and 11b). The effect of solid loading on bubble velocity is shown in Figure 16c, which implies the deceleration of bubbles by solids. It is contradictory when compared with its effect on the bubble diameter (see Figure 14c), where the coalescence rate is enhanced. It should be noted that the particle diameter utilized in this study is relatively large (Stokes number >1); thus, the interaction between bubbles and particles is dominant, even though the bubbles intend to coalesce with an increase of solids, and the kinetic energy of bubbles is reduced.[32,64] In addition, the decrease of bubble velocity near the wall at higher C_s is more rapidly, which further verifies the interaction effect of large particles with bubbles.

Conclusion

The hydrodynamics at the macro- and meso- scales, including phase holdup, liquid velocity and bubble behaviors (local gas holdup, bubble frequency, bubble diameter and bubble velocity), in a gas-liquid-solid three phase JLR operated in the pseudo-homogeneous flow regime are comprehensively experimentally investigated, which improve the understanding of dynamics in a gas-liquid-solid three phase JLR and provide benchmark data (especially the mesoscale feature, e.g., BSD) for CFD model validation. The main conclusions in this work are summarized as follows:

(1) Optical fiber probe was validated and applied in a three-phase JLR by comparing the measured bubble dynamics using a high-speed camera.

(2) The gas holdup, axial liquid velocity and bubble velocity increased with the increase of

U_g, while U_l has little influence on them.

(3) When C_s increases, the gas holdup and liquid circulation velocity decrease, and the bubble velocity also decreases due to the interaction between bubbles and particles (Stokes number>1), while the bubble diameter increases. In addition, adding solids delays the flow to reach full development.

(4) The internal circulation of bubbles and liquid flow contribute to the uniform distribution of solids, which implies the better solids suspension ability of the JLR than the slurry bubble column.

Acknowledgements

We express acknowledgment for the financial support from the National Natural Science Foundation of China (U1361112).

Notation

C_s = solid loading, dimensionless

d_b = bubble diameter, m

Eo = Eötvös number, $g\left(\rho_l-\rho_g\right)d_b^2/\sigma$

f = bubble frequency, s^{-1}

H = axial position, m

K = raw-moment, dimensionless

l_b = bubble chord length, m

L = distance between two probes, m

Mo = Morton number, $\mu_l^4\left(\rho_l-\rho_g\right)g/\left(\rho_l^2\sigma^3\right)$

N = number of segments, dimensionless

N_b = total number of bubble, dimensionless

Δp = pressure difference, Pa

$p(D)$= PDF of bubble diameter, dimensionless

r = radial position, m

R = radius of JLR, m

R_i = cross-correlation coefficient for a ith segment, dimensionless

t_i = the passing time of ith bubble through a probe tip, s

T = total sample time, s

U_g = superficial gas velocity based on reactor scale, $m \cdot s^{-1}$

U_l = superficial liquid velocity based on reactor scale, $m \cdot s^{-1}$

u_l = axial liquid velocity, $m \cdot s^{-1}$

u_b = bubble velocity, $m \cdot s^{-1}$

u_{cir} = liquid circulation velocity $\left(u_{l,r}A_r + u_{l,d}A_d\right)/\left(A_r + A_d\right)$, $m \cdot s^{-1}$

Greek letters

ε = volume fraction, dimensionless

$\overline{\varepsilon_g}$ = overall gas holdup, dimensionless

σ = surface tension, $N \cdot m^{-1}$

ρ = density, $kg \cdot m^{-3}$

μ = viscosity, $Pa \cdot s$

τ = bubble passing time through probes, s

Subscripts

g = gas phase

l = liquid phase

s = solid phase

sl =solid-liquid slurry phase

r = riser section

d = downcomer section

Literature Cited

1. Warmeling H, Behr A, Vorholt AJ. Jet loop reactors as a versatile reactor set up - Intensifying catalytic reactions: A review. *Chem Eng Sci*. 2016;149:229-248

2. Blenke H. Loop reactors. 1979:121-214

3. Sarhan AR, Naser J, Brooks G. CFD modeling of bubble column: Influence of physico-chemical properties of the gas/liquid phases properties on bubble formation. *Separation & Purification Technology*. 2018;201:130-138

4. Ojha A, Al Dahhan M. Investigation of local gas holdup and bubble dynamics using four-point optical probe technique in a split-cylinder airlift reactor. *Int J Multiphas Flow*. 2018;102:1-15

5. Gao Y, Hong D, Lu H et al. Gas holdup and liquid velocity distributions in the up flow jet-loop reactor. *Chemical Engineering Research and Design*. 2018;136:94-104

6. Gao Y, Hong D, Cheng Y, Wang L, Li X. CFD simulation for up flow jet-loop reactors by use of bi-dispersed bubble model. *Chemical Engineering Research and Design*. 2019;141:66-83

7. Sarhan AR, Naser J, Brooks G. Numerical simulation of froth formation in aerated slurry

coupled with population balance modelling. *Can Metall Quart*. 2017;56(1):45-57

8. Sarhan AR, Naser J, Brooks G. CFD model simulation of bubble surface area flux in flotation column reactor in presence of minerals. *International Journal of Mining Science and Technology*. 2018;28(6):999-1007
9. Gao X, Kong B, Vigil RD. Multiphysics simulation of algal growth in an airlift photobioreactor: Effects of fluid mixing and shear stress. *Bioresource Technol*. 2018;251:75-83
10. Gao X, Kong B, Vigil RD. Simulation of algal photobioreactors: recent developments and challenges. *Biotechnol Lett*. 2018;190(8):1-17
11. Jamshidi AM, Sohrabi M, Vahabzadeh F, Bonakdarpour B. Hydrodynamic and mass transfer characterization of a down flow jet loop bioreactor. *Biochem Eng J*. 2001;8(3):241-250
12. Fadavi A, Chisti Y. Gas holdup and mixing characteristics of a novel forced circulation loop reactor. *Chem Eng J*. 2007;131(1-3):105-111
13. Mathpati CS, Deshpande SS, Joshi JB. Computational and Experimental Fluid Dynamics of Jet Loop Reactor. *Aiche J*. 2009;55(10):2526-2544
14. Wagh SM, Koranne KV, Sonolikar RL. Operating and hydrodynamic characteristics of a reversed flow jet loop bioreactor (RFJLB) with ejector. *Bioresource Technol*. 2012;110:417-422
15. Khan Z, Joshi JB. Comparison of k－ε, RSM and LES models for the prediction of flow pattern in jet loop reactor. *Chem Eng Sci*. 2015;127:323-333
16. Heithoff S, Kück UD, Volkmer P, Fritsching U, Räbiger N. Modelling Gas‐Liquid Mass

Transfer in a Two‐Phase Jet Flow. *Can J Chem Eng*. 2018;

17. FAN LS, HWANG SJ, MATSUURA A. Hydrodynamic behavior of a draft tube gas-liquid solid spouted bed. *Chem Eng Sci*. 1984;39(12):1677-1688
18. PADMAVATHI G, RAO KR. HYDRODYNAMIC CHARACTERISTICS OF REVERSED FLOW JET LOOP REACTOR AS A GAS-LIQUID SOLID CONTACTOR. *Chem Eng Sci*. 1991;46(12):3293-3296
19. HWANG SJ, FAN LS. SOME DESIGN CONSIDERATIONS OF A DRAFT TUBE GAS-LIQUID SOLID SPOUTED BED. *CHEMICAL ENGINEERING JOURNAL AND THE BIOCHEMICAL ENGINEERING JOURNAL*. 1986;33(1):49-56
20. Pironti FF, Medina VR, Calvo R, Saez AE. Effect of draft tube position on the hydrodynamics of a draft tube slurry bubble column. *CHEMICAL ENGINEERING JOURNAL AND THE BIOCHEMICAL ENGINEERING JOURNAL*. 1995;60(1-3):155-160
21. Schluter M, Scheid S, John S, Rabiger N. Influence of local effects in three phase flows on power input in Jet-Loop Reactors. *Powder Technol*. 2005;151(1-3SI):68-76
22. Rabha S, Schubert M, Wagner M, Lucas D, Hampel U. Bubble Size and Radial Gas Hold-Up Distributions in a Slurry Bubble Column Using Ultrafast Electron Beam X-Ray Tomography. *Aiche J*. 2013;59(5):1709-1722
23. Ojima S, Hayashi K, Tomiyama A. Effects of hydrophilic particles on bubbly flow in slurry bubble column. *Int J Multiphas Flow*. 2014;58:154-167
24. Sarhan AR, Naser J, Brooks G. CFD analysis of solid particles properties effect in three-phase flotation column. *Separation & Purification Technology*. 2017;185:1-9
25. Sarhan AR, Naser J, Brooks G. Bubbly flow with particle attachment and detachment ‐

A multiphase CFD study. *Separation Science & Technology*. 2018;53(1):181-197

26. Sarhan AR. Effects of particle size and concentration on bubble coalescence and froth formation in a slurry bubble column. *Particuology*. 2018;36(1):82-95

27. Boyer C, Duquenne A, Wild G. Measuring techniques in gas – liquid and gas – liquid – solid reactors. *Chem Eng Sci*. 2002;57(16):3185-3215

28. Li H, Prakash A. Influence of slurry concentrations on bubble population and their rise velocities in a three-phase slurry bubble column. *Powder Technol*. 2000;113(1):158-167

29. Besagni G, Inzoli F. Bubble size distributions and shapes in annular gap bubble column. *Exp Therm Fluid Sci*. 2016;74:27-48

30. Maaß S, Wollny S, Voigt A, Kraume M. Experimental comparison of measurement techniques for drop size distributions in liquid/liquid dispersions. *Exp Fluids*. 2011;50(2):259-269

31. Wang TF, Wang JF, Yang WG, Jin Y. Experimental study on bubble behavior in gas-liquid-solid three-phase circulating fluidized beds. *Powder Technol*. 2003;137(1-2):83-90

32. Manjrekar ON, Dudukovic MP. Application of a 4-point optical probe to a Slurry Bubble Column Reactor. *Chem Eng Sci*. 2015;131:313-322

33. Guan X, Yang N. Bubble properties measurement in bubble columns: From homogeneous to heterogeneous regime. *Chem Eng Res Des*. 2017;127:103-112

34. Tyagi P, Buwa VV. Experimental characterization of dense gas-liquid flow in a bubble column using voidage probes. *Chem Eng J*. 2017;308:912-928

35. Besagni G, Brazzale P, Fiocca A, Inzoli F. Estimation of bubble size distributions and shapes in two-phase bubble column using image analysis and optical probes. *Flow Meas*

Instrum. 2016;52:190-207

36. Clark NN, Turton R. Chord Length Distributions Related to Bubble Size Distributions in Multiphase Flows. *Int J Multiphas Flow*. 1988;14(4):413-424

37. Liu W, Clark NN. Relationships between distributions of chord lengths and distributions of bubble sizes including their statistical parameters. *Int J Multiphas Flow*. 1995;21(6):1073-1089

38. Santana D, Rodriguez-Rodriguez J, Almendros-Ibanez JA, Martinez-Bazan C. Characteristic lengths and maximum entropy estimation from probe signals in the ellipsoidal bubble regime. *Int J Multiphas Flow*. 2006;32(9):1123-1139

39. Guan X, Gao Y, Tian Z et al. Hydrodynamics in bubble columns with pin-fin tube internals. *Chem Eng Res Des*. 2015;102:196-206

40. Gandhi B, Prakash A, Bergougnou MA. Hydrodynamic behavior of slurry bubble column at high solids concentrations. *Powder Technol*. 1999;103(2):80-94

41. Yang S, Li X, Yang C, Ma B, Mao Z. Computational Fluid Dynamics Simulation and Experimental Measurement of Gas and Solid Holdup Distributions in a Gas-Liquid-Solid Stirred Reactor. *Ind Eng Chem Res*. 2016;55(12):3276-3286

42. Zhang K. Axial solid concentration distribution in tapered and cylindrical bubble columns. *Chem Eng J*. 2002;86(PII S1385-8947(01)00190-53):299-307

43. Sun SL, Liu CJ, Wei WS, Bao XJ. Hydrodynamics of an annulus airlift reactor. *Powder Technol*. 2006;162(3):201-207

44. Forret A, Schweitzer JM, Gauthier T, Krishna R, Schweich D. Influence of scale on the hydrodynamics of bubble column reactors: an experimental study in columns of 0.1, 0.4 and

1 m diameters. *Chem Eng Sci*. 2003;58(3-6):719-724

45. Li Z, Guan X, Wang L, Cheng Y, Li X. Experimental and numerical investigations of scale-up effects on the hydrodynamics of slurry bubble columns. *Chinese J Chem Eng*. 2016;24(8):963-971

46. Li X, Yang C, Yang S, Li G. Fiber-Optical Sensors: Basics and Applications in Multiphase Reactors. *Sensors-Basel*. 2012;12(9):12519-12544

47. Gao Y, Gao X, Wu C et al. Novel phase inversion model for gas-solid turbulent fluidized beds. *Powder Technol*. 2015;283:344-354

48. Razzak SA, Barghi S, Zhu JX, Mi Y. Phase holdup measurement in a gas-liquid-solid circulating fluidized bed (GLSCFB) riser using electrical resistance tomography and optical fibre probe. *Chem Eng J*. 2009;147(2-3):210-218

49. Lo CS, Hwang SJ. Local hydrodynamic properties of gas phase in an internal-loop airlift reactor. *Chem Eng J*. 2003;91(PII S1358-8947(02)00042-61):3-22

50. Liu M, Zhang Y, Bi H, Grace JR, Zhu Y. Non-intrusive determination of bubble size in a gas-solid fluidized bed: An evaluation. *Chem Eng Sci*. 2010;65(11):3485-3493

51. Sobrino C, Almendros-Ibanez JA, Santana D, Vazquez C, de Vega M. Maximum entropy estimation of the bubble size distribution in fluidized beds. *Chem Eng Sci*. 2009;64(10):2307-2319

52. Acosta-Iborra A, Sobrino C, Hernandez-Jimenez F, de Vega M. Experimental and computational study on the bubble behavior in a 3-D fluidized bed. *Chem Eng Sci*. 2011;66(15):3499-3512

53. Bozzano G, Dente M. Shape and terminal velocity of single bubble motion: a novel

approach. *Comput Chem Eng*. 2001;25(4-6):571-576

54. Ramezani M, Kong B, Gao X, Olsen MG, Vigil RD. Experimental measurement of oxygen mass transfer and bubble size distribution in an air‐water multiphase Taylor‐Couette vortex bioreactor. *Chem Eng J*. 2015;279:286-296

55. Jia X, Wen J, Feng W, Yuan Q. Local hydrodynamics modeling of a gas-liquid-solid three-phase airlift loop reactor. *Ind Eng Chem Res*. 2007;46(15):5210-5220

56. Schallenberg J, Enss JH, Hempel DC. The important role of local dispersed phase hold-ups for the calculation of three-phase bubble columns. *Chem Eng Sci*. 2005;60(22SI):6027-6033

57. Mena PC, Ruzicka MC, Rocha FA, Teixeira JA, Drahos J. Effect of solids on homogeneous-heterogeneous flow regime transition in bubble columns. *Chem Eng Sci*. 2005;60(22SI):6013-6026

58. Razzak SA, Barghi S, Zhu JX. Electrical resistance tomography for flow characterization of a gas-liquid-solid three-phase circulating fluidized bed. *Chem Eng Sci*. 2007;62(24SI):7253-7263

59. MUROYAMA K, FAN LS. FUNDAMENTALS OF GAS-LIQUID-SOLID FLUIDIZATION. *Aiche J*. 1985;31(1):1-34

60. Siegel MH, Merchuk JC, Schugerl K. Air‐lift reactor analysis: Interrelationships between riser, downcomer, and gas‐liquid separator behavior, including gas recirculation effects. *Aiche J*. 1986;32(10):1585‐1596

61. Akita K, Yoshida F. Gas holdup and volumetric mass transfer coefficient in bubble columns. Effects of liquid properties. *Industrial & Engineering Chemistry Process Design and Development*. 1973;12(1):76-80

62. Krishna R, DeSwart J, Ellenberger J, Martina GB, Maretto C. Gas holdup in slurry bubble columns: Effect of column diameter and slurry concentrations. *Aiche J*. 1997;43(2):311-316

63. Sarhan AR, Naser J, Brooks G. CFD simulation on influence of suspended solid particles on bubbles' coalescence rate in flotation cell. *Int J Miner Process*. 2016;146:54-64

64. Hooshyar N, van Ommen JR, Hamersma PJ, Sundaresan S, Mudde RF. Dynamics of Single Rising Bubbles in Neutrally Buoyant Liquid-Solid Suspensions. *Phys Rev Lett*. 2013;110(24450124)

Figure captions

Figure 1. Schematic diagram of the JLR.

Figure 2. Representative signals for the gas-liquid and gas-liquid-solid system by PV6D.

Figure 3. Signal processing for optical fiber probe in a segment (U_g=0.065 m/s, U_l=0.01 m/s, C_s=5 %vol., data length= 4096): (a) typical normalized signals of two probes, where signals above the baseline (dot dash line) represent to bubbles, and in enlarged view, t_i represents a bubble passing time though the leading probe; (b) threshold determination by PDF method; (c) cross-correlation function R_{xy} method, where τ_i in enlarged view represents the dwelling time of the bubble passing through probes.

Figure 4. Optical fiber probe validation experiment using a high-speed camera: (a) schematic diagram of 2-D bubble column; (b) needle sparger; (c) typical photograph.

Figure 5. Comparison results by an optical fiber probe and a high-speed camera (U_g= 0.0287 m/s): (a) bubble velocity PDF; (b) BSD.

Figure 6. Effect of solid loading on overall gas holdup and liquid circulation velocity (U_g = 0.085 m/s, U_l =0.01 m/s).

Figure 7. Radial solid holdup profiles at different heights under U_g = 0.125 m/s, U_l =0.01 m/s, C_s=30 vol.%, where H=1.65 m and 1.9 m belong to the separator section.

Figure 8. Effects of (a) U_g (U_l =0.01 m/s); (b) U_l (U_g = 0.125 m/s) on axial solid holdup distributions at C_s=30 vol.%.

Figure 9. Effect of C_s on radial solid holdup distributions (U_g = 0.125 m/s, U_l =0.01 m/s, H=0.65 m).

Figure 10. Radial profiles of axial liquid velocity considered the effects of: (a) U_g (U_l = 0.01

m/s, C_s = 5 vol.%, H = 1.15 m); (b) U_l (U_g = 0.065 m/s, C_s = 5 vol.%, H = 1.15 m); (c) C_s (U_g = 0.085 m/s, U_l = 0.01 m/s, H = 0.65 m).

Figure 11. Radial profiles of local gas holdup considered the effects of: (a) U_g (U_l = 0.01 m/s, C_s = 5 vol.%); (b) U_l (U_g = 0.065 m/s, C_s = 5 vol.%); (c) C_s (U_g = 0.085 m/s, U_l = 0.01 m/s) at H = 1.15 m.

Figure 12. Axial evolutions of local gas holdup at two solid loadings: (a) C_s = 5 vol.%; (b) C_s = 30 vol.%, under U_g = 0.085 m/s, U_l = 0.01 m/s.

Figure 13. Radial profiles of bubble frequency considered the effects of: (a) U_g (U_l = 0.01 m/s, C_s = 5 vol.%); (b) U_l (U_g = 0.065 m/s, C_s = 5 vol.%); (c) C_s (U_g = 0.085 m/s, U_l = 0.01 m/s) at H = 1.15 m.

Figure 14. Effects of: (a) U_g (U_l = 0.01 m/s, C_s = 5 vol.%); (b) U_l (U_g = 0.065 m/s, C_s = 5 vol.%); (c) C_s (U_g = 0.085 m/s, U_l = 0.01 m/s) on (i) BSD (at r/R = 0) and (ii) radial profiles of mean bubble diameter at H = 1.15 m.

Figure 15. BSDs for different radial positions under U_g = 0.085 m/s, U_l = 0.01 m/s, C_s = 5 vol.%, H = 1.15 m, where r/R = 0.77 is located at the downcomer.

Figure 16. Radial profiles of bubble velocity considered the effects of: (a) U_g (U_l = 0.01 m/s, C_s = 5 vol.%); (b) U_l (U_g = 0.065 m/s, C_s = 5 vol.%); (c) C_s (U_g = 0.085 m/s, U_l = 0.01 m/s) at H = 1.15 m.

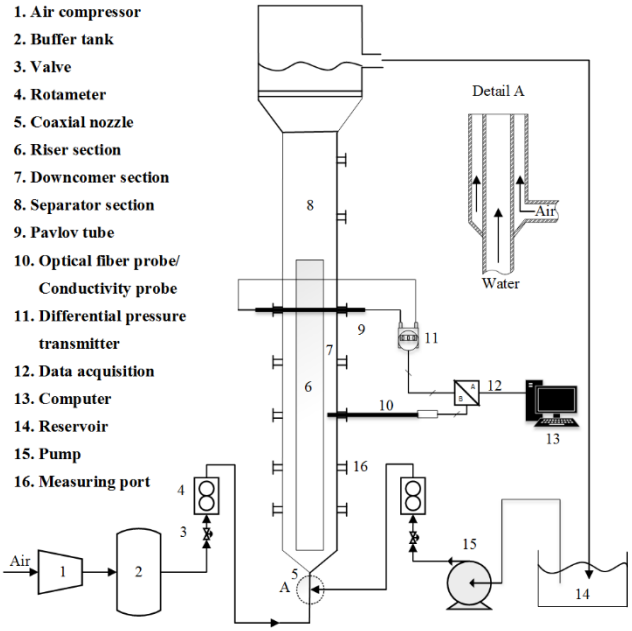

Figure 1. Schematic diagram of the JLR.

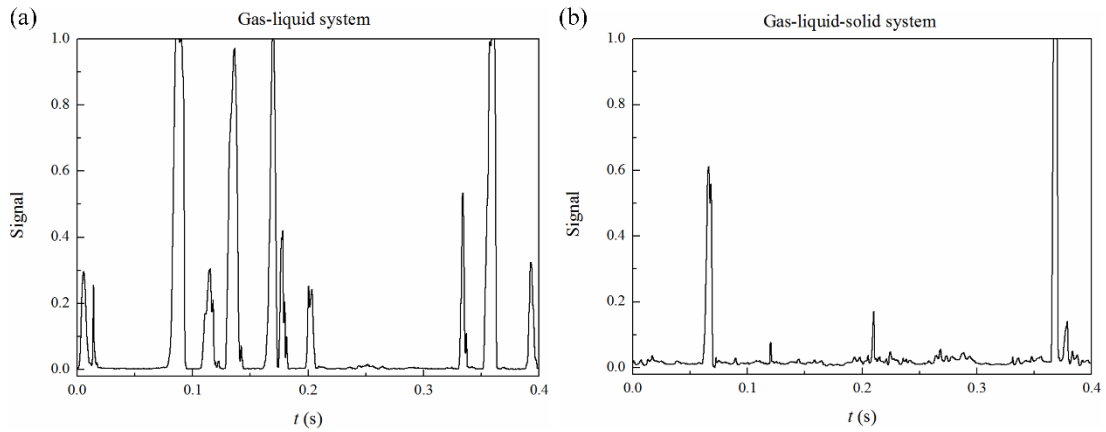

Figure 2. Representative signals for the gas-liquid and gas-liquid-solid system by PV6D.

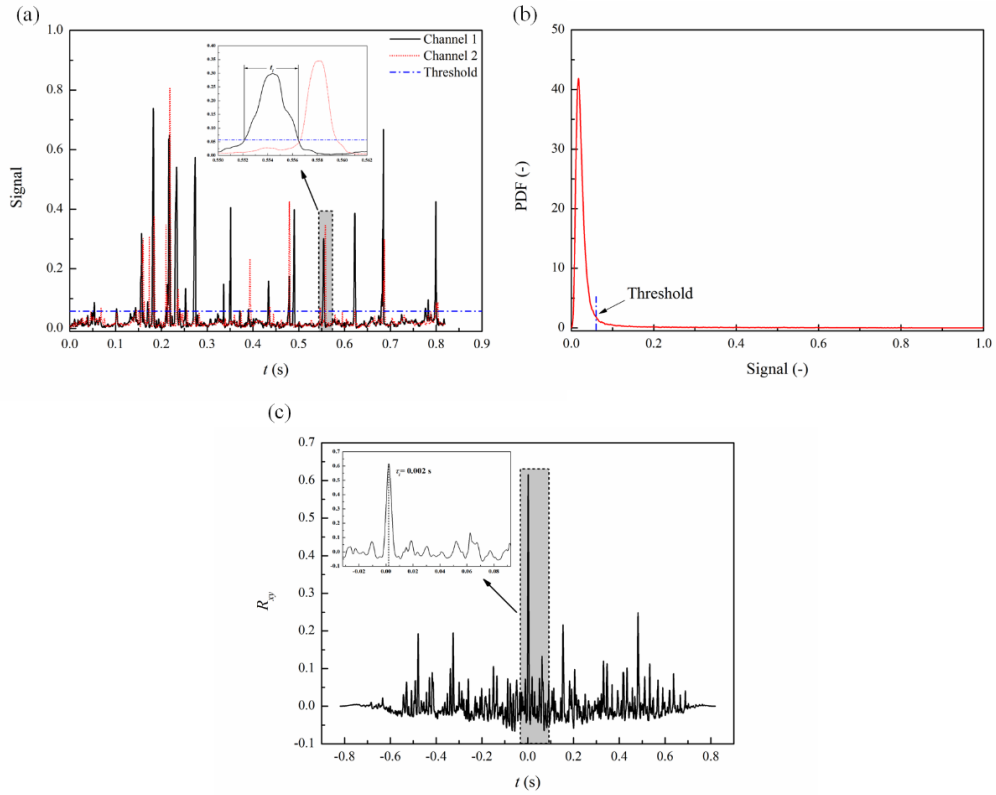

Figure 3. Signal processing for optical fiber probe in a segment (U_g=0.065 m/s, U_l=0.01 m/s, C_s=5 %vol., data length= 4096): (a) typical normalized signals of two probes, where signals above the baseline (dot dash line) represent to bubbles, and in enlarged view, t_i represents a bubble passing time though the leading probe; (b) threshold determination by PDF method; (c) cross-correlation function R_{xy} method, where τ_i in enlarged view represents the dwelling time of the bubble passing through probes.

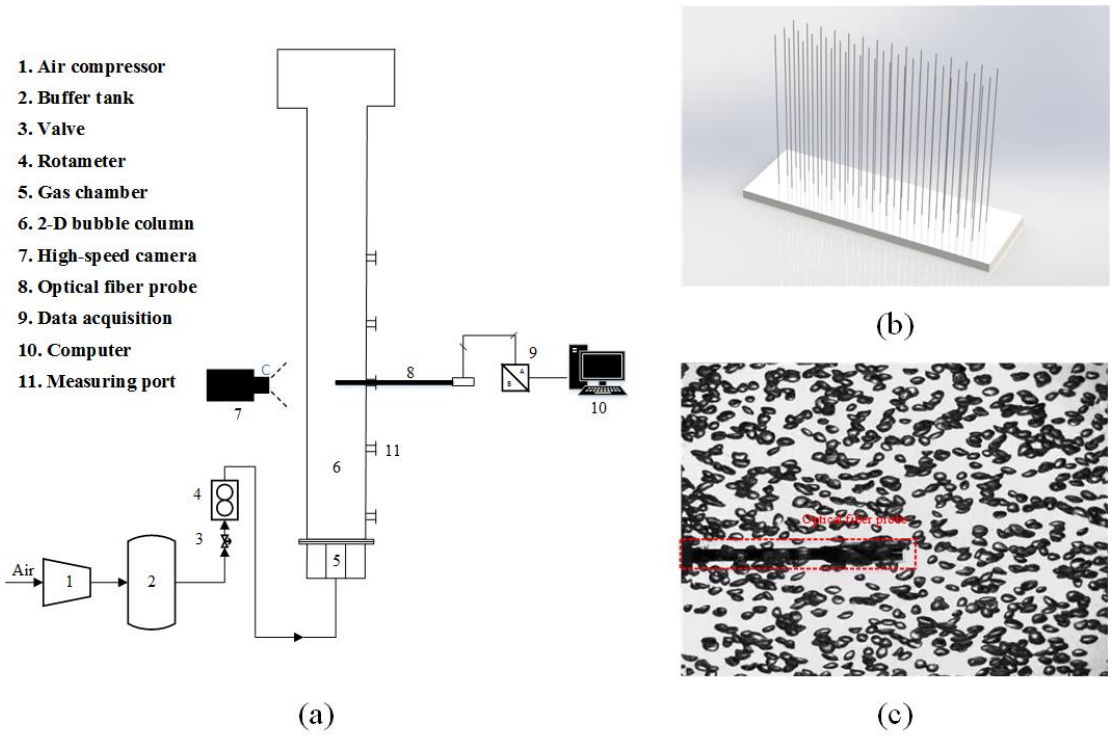

Figure 4. Optical fiber probe validation experiment using a high-speed camera: (a) schematic diagram of 2-D bubble column; (b) needle sparger; (c) typical photograph.

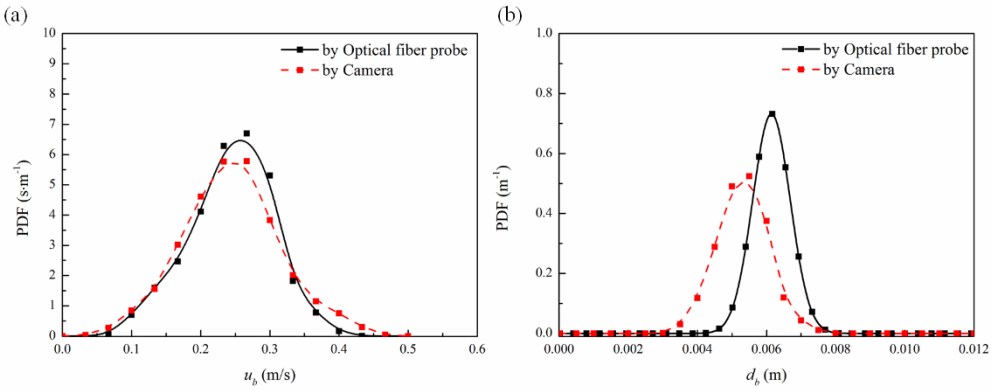

Figure 5. Comparison results by an optical fiber probe and a high-speed camera (U_g= 0.0287 m/s): (a) bubble velocity PDF; (b) BSD.

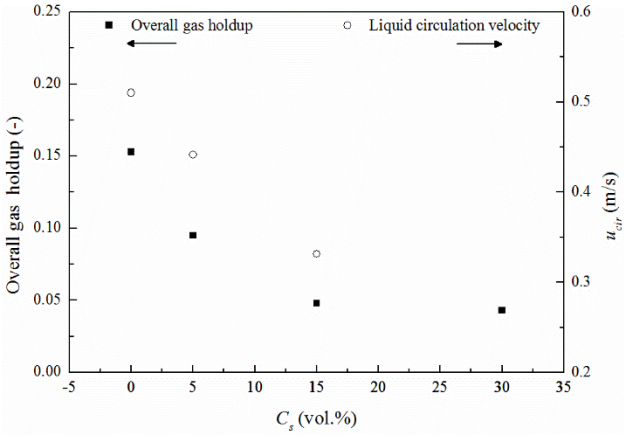

Figure 6. Effect of solid loading on overall gas holdup and liquid circulation velocity (U_g = 0.085 m/s, U_l =0.01 m/s).

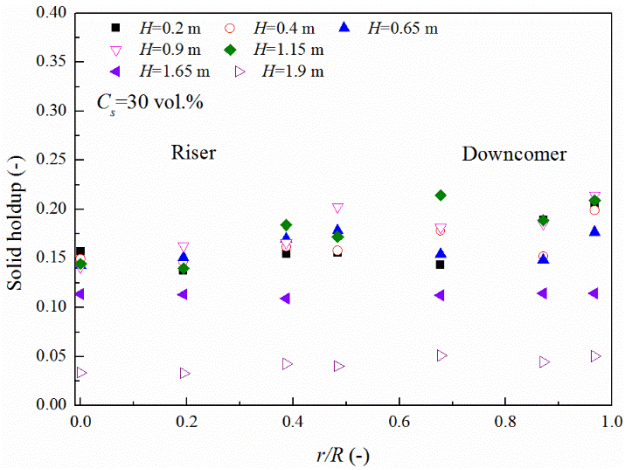

Figure 7. Radial solid holdup profiles at different heights under U_g = 0.125 m/s, U_l =0.01 m/s, C_s=30 vol.%, where H=1.65 m and 1.9 m belong to the separator section.

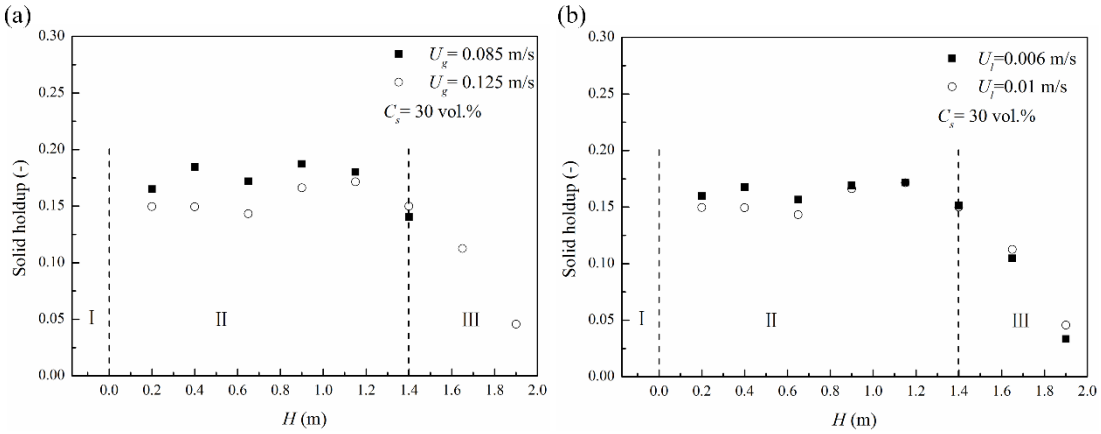

Figure 8. Effects of (a) U_g (U_l=0.01 m/s); (b) U_l (U_g = 0.125 m/s) on axial solid holdup distributions at C_s=30 vol.%.

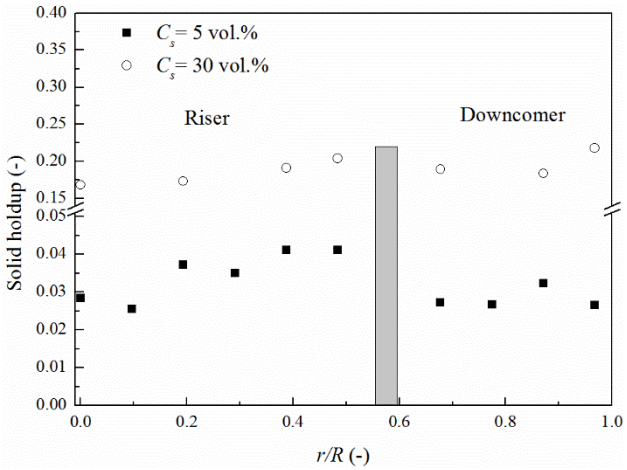

Figure 9. Effect of C_s on radial solid holdup distributions (U_g = 0.125 m/s, U_l =0.01 m/s, H=0.65 m).

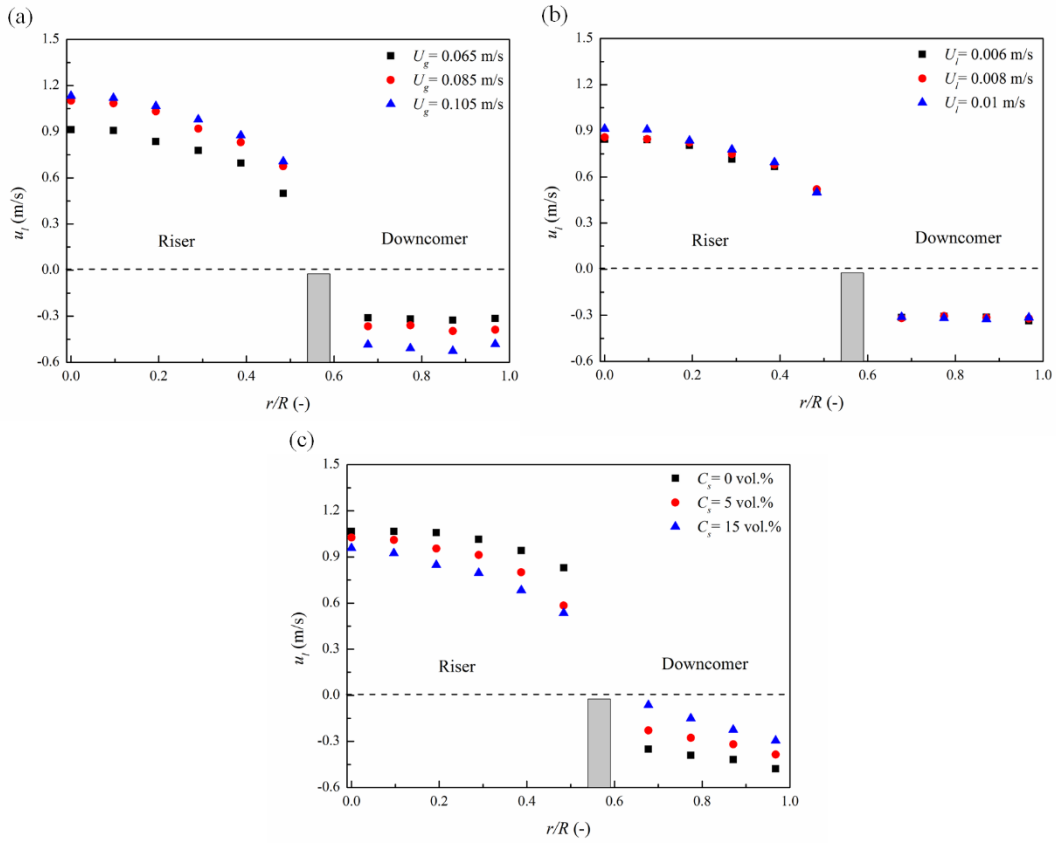

Figure 10. Radial profiles of axial liquid velocity considered the effects of: (a) U_g (U_l = 0.01 m/s, C_s = 5 vol.%, H = 1.15 m); (b) U_l (U_g = 0.065 m/s, C_s = 5 vol.%, H = 1.15 m); (c) C_s (U_g = 0.085 m/s, U_l = 0.01 m/s, H = 0.65 m).

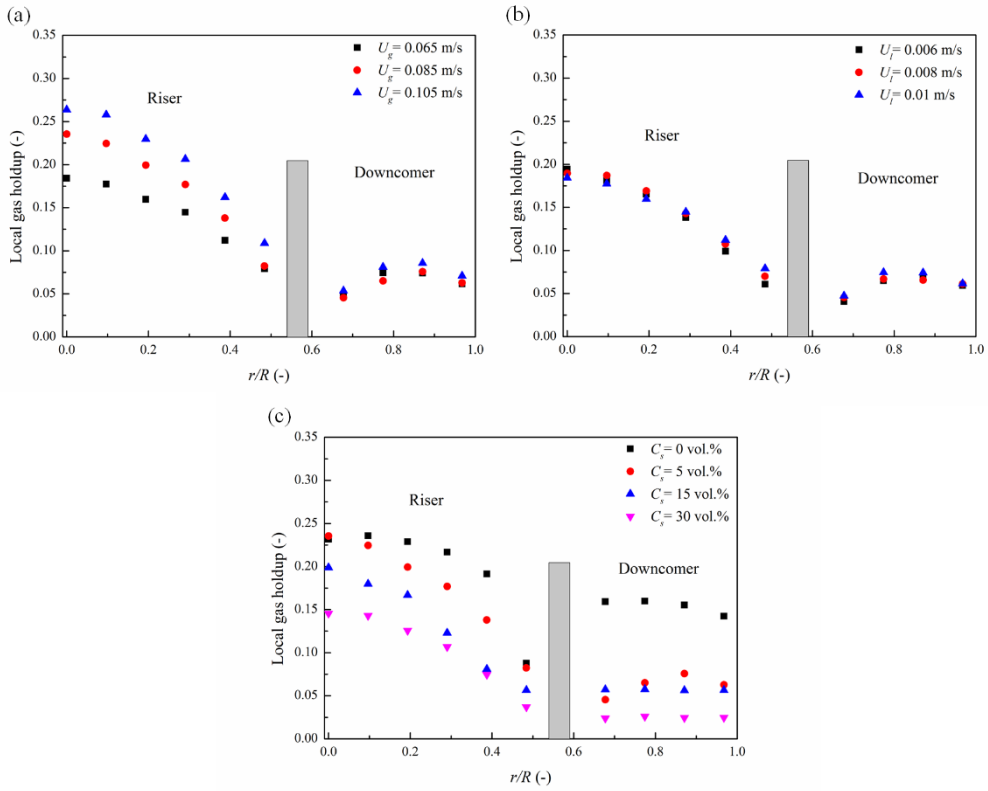

Figure 11. Radial profiles of local gas holdup considered the effects of: (a) U_g (U_l = 0.01 m/s, C_s = 5 vol.%); (b) U_l (U_g = 0.065 m/s, C_s = 5 vol.%); (c) C_s (U_g = 0.085 m/s, U_l = 0.01 m/s) at H = 1.15 m.

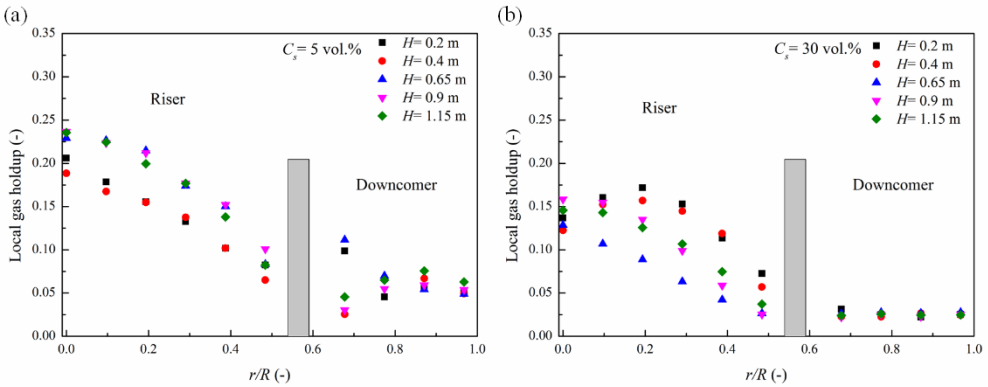

Figure 12. Axial evolutions of local gas holdup at two solid loadings: (a) C_s = 5 vol.%; (b) C_s = 30 vol.%, under U_g = 0.085 m/s, U_l = 0.01 m/s.

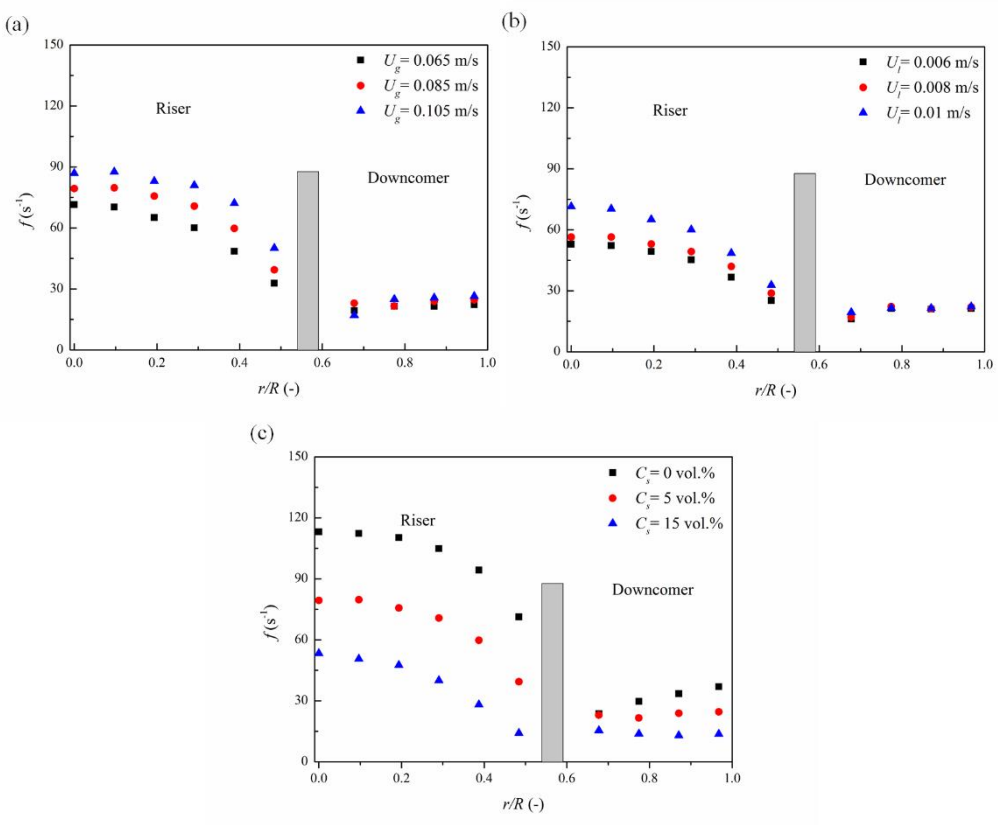

Figure 13. Radial profiles of bubble frequency considered the effects of: (a) U_g (U_l = 0.01 m/s, C_s = 5 vol.%); (b) U_l (U_g = 0.065 m/s, C_s = 5 vol.%); (c) C_s (U_g = 0.085 m/s, U_l = 0.01 m/s) at H = 1.15 m.

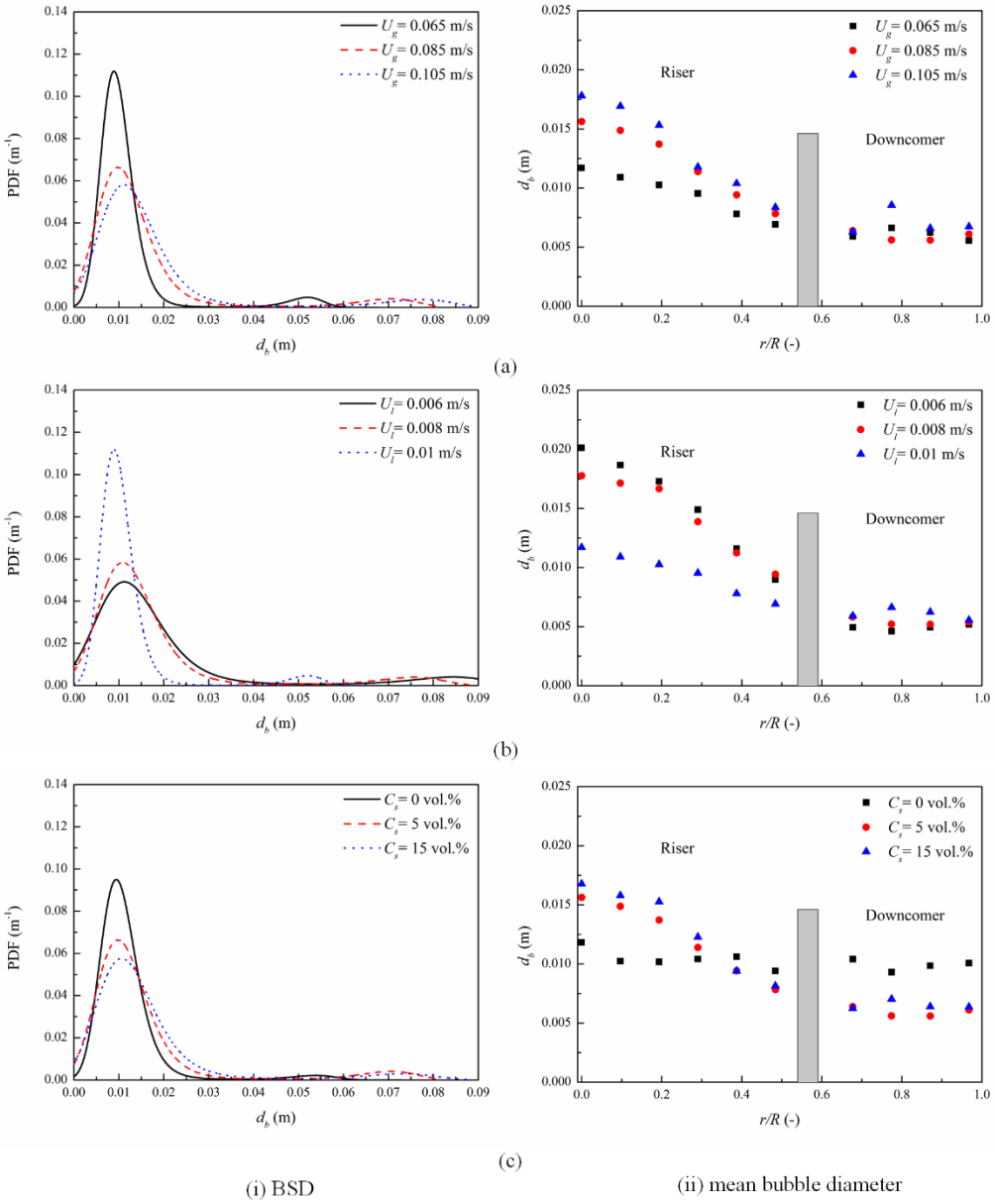

Figure 14. Effects of: (a) U_g (U_l = 0.01 m/s, C_s = 5 vol.%); (b) U_l (U_g = 0.065 m/s, C_s = 5 vol.%); (c) C_s (U_g = 0.085 m/s, U_l = 0.01 m/s) on (i) BSD (at r/R = 0) and (ii) radial profiles of mean bubble diameter at H = 1.15 m.

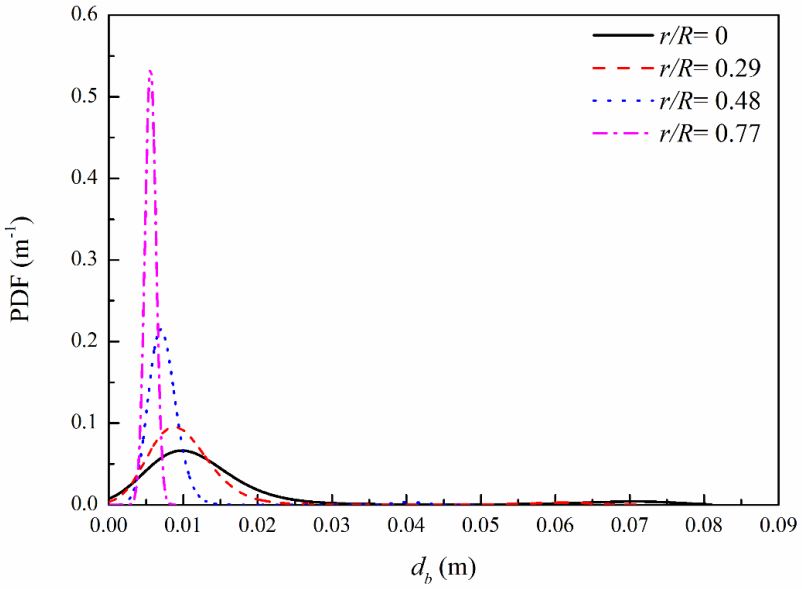

Figure 15. BSDs for different radial positions under U_g = 0.085 m/s, U_l = 0.01 m/s, C_s = 5 vol.%, H = 1.15 m, where r/R= 0.77 is located at the downcomer.

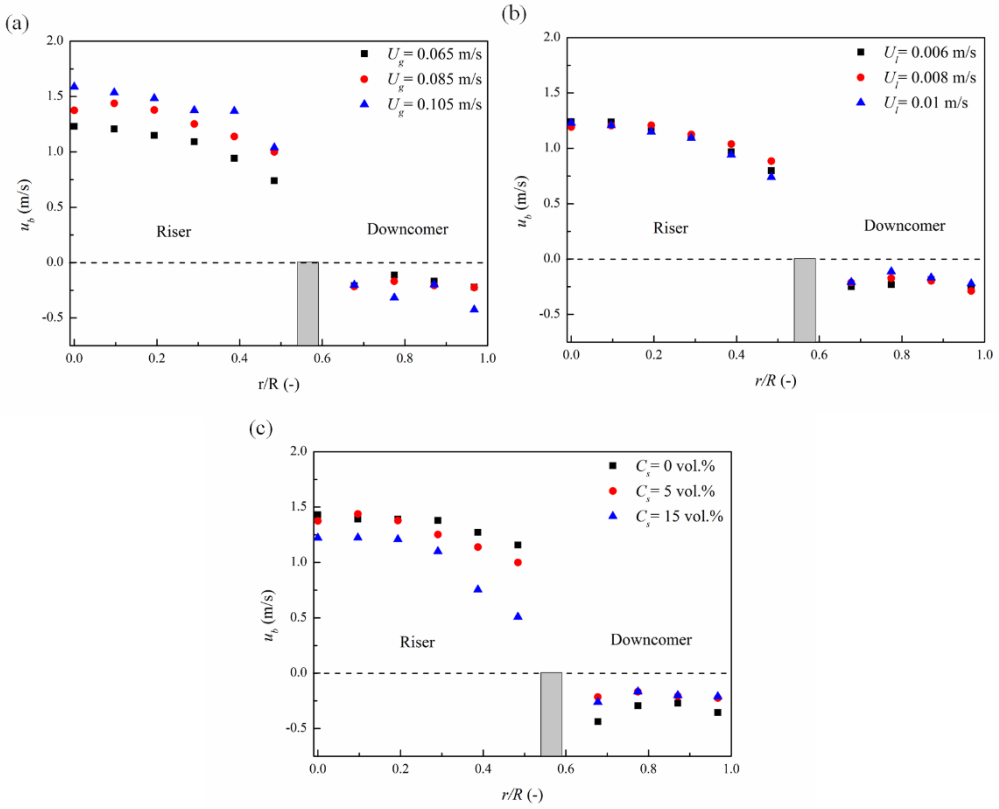

Figure 16. Radial profiles of bubble velocity considered the effects of: (a) U_g (U_l = 0.01 m/s, C_s = 5 vol.%); (b) U_l (U_g = 0.065 m/s, C_s = 5 vol.%); (c) C_s (U_g = 0.085 m/s, U_l = 0.01 m/s) at H = 1.15 m.

Table 1. Experimental operation conditions

Item	Operation condition
Superficial gas velocity, U_g (m/s)	0.065, 0.085, 0.105, 0.125
Superficial liquid velocity, U_l (m/s)	0.006, 0.008, 0.01
Solid loading, C_s (vol.%)	0, 5, 15, 30
Axial heights, H (m)	0.2, 0.4, 0.65, 0.9, 1.15, 1.6, 1.9
Radial positions, r/R	Riser section (0, 0.096, 0.19, 0.29, 0.39, 0.48); Downcomer section (0.68, 0.77, 0.87, 0.97)

Table 2. Validation results of Optical fiber probe compared with camera

$U_g \times 10^{-2}$ (m/s)	$\overline{\varepsilon_g}$	u_b (m/s)			$d_b \times 10^3$ (m)		
		Camera	OP	RE (%)	Camera	OP	RE (%)
0.92	0.043	0.261	0.225	-13.79	3.623	4.168	15.04
2.27	0.117	0.226	0.208	-7.96	4.676	5.158	10.31
2.87	0.139	0.244	0.221	-9.43	5.159	5.817	12.75

$$\mathrm{RE} = \frac{\psi_{\mathrm{OP}} - \psi_{\mathrm{Camera}}}{\psi_{\mathrm{Camera}}} \times 100 \left(\psi = u_b \text{ or } d_b \right)$$